ROYAL SOCIETY OF CHEMISTRY

PAPER

Check for updates

Novel highly efficient Bi^{3+}-activated phosphors for warm WLEDs

Xiudi Wu,[ab] Xibao Zhang,[ab] Yonghui Xu,[ab] Shuwen Yin,[a] Chuansheng Zhong,[ab] Liang Zhou [ID] *[ab] and Hongpeng You [ID] *[abc]

In this paper, novel Bi^{3+}-activated $Ca_2LuZrScAl_2GeO_{12}$ (CLZSAG) phosphors with a garnet structure were prepared by a high temperature solid-state method. There are two kinds of luminescent centers in the CLZSAG:Bi^{3+} phosphors, which exhibit a blue emission under 365 nm excitation and a rare near-ultraviolet emission with a narrow band (FWHM = 34 nm) under 290 nm excitation. The combination of the structure and luminescence reveals that the Bi^{3+} ions occupy the sites of the LuO_8 and ScO_6 polyhedra with different local coordination environments, leading to two different luminescence behaviors. In addition, the prepared phosphors also have excellent thermostability ($I_{423K/298K} = 80\%$), and high quantum efficiencies of 72% and 60% under 290 and 365 nm excitation, respectively. Since the absorption band of the phosphor in the UV-visible region can match well with the commercial 365 nm chips, a high-performance WLED device with a high color rendering index ($R_a = 98.5$) and a low correlated color temperature (CCT = 4455 K) was obtained by combining commercial phosphors Lu-YAG:Ce^{3+} and $CaAlSiN_3$:Eu^{2+} and samples of the CLZSAG:Bi^{3+} phosphor with 365 nm chips. Our results demonstrate that CLZSAG:Bi^{3+} has great potential application in WLED devices.

Introduction

Since mankind lit the world's first fire, the pursuit of more environmentally friendly and efficient light sources has never stopped. With the improvement of people's living standards and energy utilization efficiency, the application of various artificial lighting devices, from incandescent lamps to halogen lamps, xenon lamps, fluorescent lamps, and white light emitting diodes (WLEDs), is continuously driving the development of lighting technology.[1–9] Compared with traditional light sources, phosphor-converted WLED (pc-WLED) technology has become the dominant light source because of its advantages of high efficiency, environmental protection, fast response time, and small volume.[10–17] Considering the application needs of various fields, there is still great room for the progress of pc-WLED technology. The color rendering index (CRI) is an important parameter to evaluate the quality of pc-WLEDs, and the higher the CRI, the better the color reproduction.[18–21] Currently, the commercially available fabrication technique for pc-WLEDs is based on the combination of

the blue LED chip (440–480 nm), $CaAlSiN_3$:Eu^{2+} red phosphor and Lu/Ga-YAG:Ce^{3+} yellow-green phosphor. However, the prepared LED devices are limited in their applicability due to their low CRI ($\sim$82) and high CCT ($>$4500 K) values.[7,22–26] Therefore, other production techniques for pc-WLEDs have occasionally been developed, involving the use of near-UV LED chips and trichromatic (red, green and blue) phosphors. Surprisingly, near-UV excited pc-WLEDs can easily achieve warm white light with a high CRI. High CRI values ($>$90) can satisfy the demands of certain spaces with high color requirements, such as libraries, cinemas, art galleries, jewellery, surgeries and cosmetic sales counters, making high CRI values an important standard in lighting displays.[3,27,28]

As one of the most crucial components of pc-WLEDs, blue light-emitting phosphors greatly affect the performance of lighting equipment. Previous studies on blue phosphors were focused on rare earth metal ions (Ce^{3+} and Eu^{2+}) due to the controlled luminescence color and high quantum yields, which resulted from the 4f–5d electronic transitions.[29] Previous reports on Ce^{3+} and Eu^{2+} activated blue light-emitting phosphors are common, such as $BaGa_2Si_2O_8$:Ce^{3+} and Na_3KMg_7-$(PO_4)_6$:Eu^{2+}.[30,31] However, the emission spectrum of the Eu^{2+}-doped phosphor is not sufficiently wide to adequately fill the cyan gap. Some Ce^{3+}-doped phosphors still have drawbacks such as low quantum efficiency and poor thermal stability, such as $BaCa_2Y_6O_{12}$:Ce^{3+} ($I_{423K}/I_{298K} = 4.8\%$),[32] $Sr_3Sc_4O_9$:Ce^{3+} ($I_{423K}/I_{298K} = 19.1\%$),[33] $BaLa_2Si_2S_8$:Ce^{3+} (IQE: 36.07%),[34] and

[a] State Key Laboratory of Rare Earth Resource Utilization, Changchun Institute of Applied Chemistry, Chinese Academy of Sciences, Changchun 130022, P. R. China. E-mail: zhoul@ciac.ac.cn, hpyou@ciac.ac.cn; Fax: +86 431 85698041

[b] University of Science and Technology of China, Hefei 230026, P. R. China

[c] Ganjiang Innovation Academy, Chinese Academy of Sciences, Ganzhou 341000, China

$YScSi_4N_6C:Ce^{3+}$ (IQE: 30.3%).[35] In addition, blue phosphors should have a strong absorption in the UV-visible region to ensure a match with the near-UV-excited chip. Excellent thermal stability and internal photoluminescence (PL) quantum efficiency are the most critical factors related to the overall electro-optical conversion efficiency of packaged white LEDs.[36–38] Consequently, it is still a considerable challenge to seek excellent blue phosphors with near-UV absorption.

Herein, we designed and synthesized new $Ca_2LuZrScAl_2GeO_{12}:Bi^{3+}$ (CLZSAG:Bi^{3+}) phosphors with a garnet structure. The crystal structure, quantum efficiency, luminescence properties, optimal doping concentration, lifetime and temperature-dependent spectra were systematically investigated. There are two kinds of luminescent centers in the CLZSAG:Bi^{3+} phosphor, which gives blue and near-ultraviolet emissions with a narrow band (FWHM = 34 nm) under different excitations. These luminescence behaviors can be ascribed to the site occupation of the Bi^{3+} ions in LuO_8 and ScO_6 polyhedrons with different local coordination environments. Furthermore, a high-performance warm WLED device with a high color rendering index (R_a = 98.5) and a low correlated color temperature (CCT = 4455 K) was fabricated by combining commercial yellow-green phosphor Lu-YAG:Ce^{3+}, prepared blue phosphor CLZSAG:0.14Bi^{3+} and red phosphor $CaAlSiN_3:Eu^{2+}$ with 365 nm near-UV LED chips.

Experimental section

Materials and synthesis

A series of samples of CLZSAG:xBi^{3+} (x = 0–0.25) were prepared using the conventional solid-state reaction route. In the first step, the raw materials $CaCO_3$ (99.9%), Lu_2O_3 (99.99%), Sc_2O_3 (99.9%), ZrO_2 (99.9%), Al_2O_3 (99.9%), GeO_2 (99.99%), and Bi_2O_3 (99.999%) were weighed according to the stoichiometric ratio. After 30 minutes of grinding, the raw materials were transferred to the alumina crucible and heated in a muffle furnace at 1500 °C for 4 hours under air atmosphere. After the reaction, the final samples were ground into fine powder and collected for further characterization.

Characterization

X-ray diffraction (XRD) patterns, scanning electron microscopy (SEM), excitation and emission spectrum measurements, temperature-dependent emission spectrum determination, fluorescence lifetime and quantum efficiency tests were described in detail in our team's previous work.[39,40] The photoelectric performances of pc-LEDs were measured using Starspec SSP6612 instruments.

LED fabrication

The prepared blue phosphor CLZSAG:0.14Bi^{3+}, commercial yellow-green phosphor Lu-YAG:Ce^{3+} and red phosphor $CaAlSiN_3:Eu^{2+}$ were mixed with epoxy resin (A : B = 1 : 1) for 40 min to form a composite solution. The pc-wLED was fabricated by uniformly coating the composite solution on the 365 nm chip

and drying it at 353 K. The optical properties of the fabricated WLED lamp were measured at an operating current of 20–120 mA.

Results and discussion

Structure and morphology

In order to investigate the luminescence properties of the Bi^{3+} ions in the host materials, we prepared a set of CLZSAG:xBi^{3+} phosphors. As shown in Fig. 1a, all diffraction peaks match well with the data on the standard card, and no impurity phase has been detected, indicating that the Bi^{3+} ions were successfully introduced into the CLZSAG host without altering the crystal structure.[41] The structure is refined by XRD Rietveld refinement, where the structure of CLZSAG is used as the initial model of refinement, as shown in Fig. 1b. The Rietveld refinement results show that the sample is isomorphic with CLZSAG and no impurity phase is detected. The detailed structural parameters and crystallographic data of CLZSAG and CLZSAG:0.04Bi^{3+} components are given in Table 1. The low R factor value shows that the Rietveld refining result is reliable (Table 1).

Fig. 1c shows that the CLZSAG:0.14Bi^{3+} phosphor possesses a garnet structure with a $Ia\bar{3}d$ (230) space group. As a typical non-rare earth activator ion, Bi^{3+} ions can emit in the range of ultraviolet to near-infrared due to the influence of the coordination environment in the host materials. Ca^{2+}/Lu^{3+}, Sc^{3+}/Zr^{4+}, and Al^{3+}/Ge^{4+} cations are coordinated by eight, six and four surrounding O^{2-} to form a dodecahedron, an octahedron and a tetrahedron, respectively. In addition, the $[(Ca/Lu)O_8]$
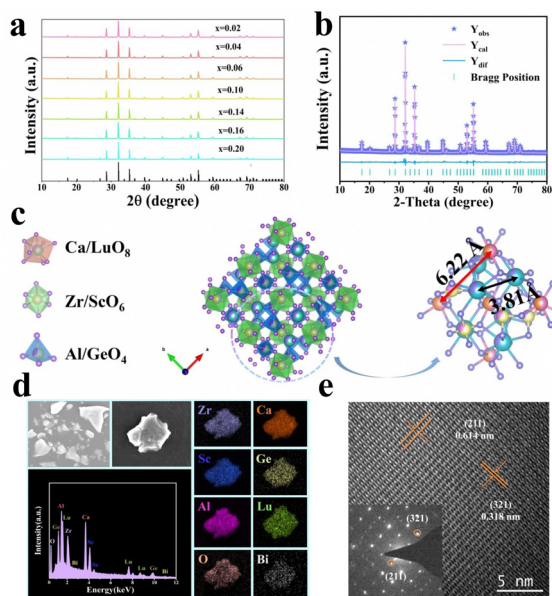

Fig. 1 (a) XRD patterns of the CLZSAG:xBi^{3+} samples (2θ = 10–80°). (b) Rietveld refinement of CLZSAG:0.04Bi^{3+}. (c) Crystal structure of CLZSAG. (d) SEM images, EDS spectrum and elemental maps of the CLZSAG:0.14Bi^{3+} sample. (e) High-resolution TEM (HRTEM) images of the CLZSAG:0.14Bi^{3+} sample; the inset shows the selected area electron diffraction patterns.

This journal is © The Royal Society of Chemistry 2023

J. Mater. Chem. C, 2023, **11**, 8818–8825 | **8819**

Table 1 Refined crystallographic parameters of the samples: the CLZSAG host and CLZSAG:0.04Bi^{3+}

Compound	Ca$_2$LuZrScAl$_2$GeO$_{12}$:0.04Bi^{3+}	Ca$_2$LuZrScAl$_2$GeO$_{12}$
Space group	$Ia\bar{3}d$ (230)	$Ia\bar{3}d$ (230)
Symmetry	Cubic	Cubic
$a = b = c$/Å	12.460	12.440
V Å^{-3}	1934.561	1930.017
$\alpha = \beta = \gamma$	90°	90°
Z	8	8
R_{wp}, %	7.17	8.28
R_p, %	4.97	6.12
χ^2	4.99	7.17

dodecahedron are connected to the [(Al/Ge)O$_4$] tetrahedron and the [(Sc/Zr)O$_6$] octahedron by sharing edges. Namely, Zr^{4+}/Sc^{3+} or Al^{3+}/Ge^{4+} can affect the coordination environment of the dodecahedron site, thus affecting the luminescence of Bi^{3+} ions. According to the previously reported CLZSAG crystal, there are six types of cations.[41] Wherein, the ionic radius of Ca^{2+} is 1.12 Å (CN = 8, CN: coordination number), Lu^{3+} is 0.977 Å (CN = 8), Zr^{4+} is 0.72 Å (CN = 6), Sc^{3+} is 0.745 Å (CN = 6), Al^{3+} is 0.39 Å (CN = 4), Ge^{4+} is 0.73 Å (CN = 4), and Bi^{3+} are 1.03 Å (CN = 6) and 1.17 Å (CN = 8), respectively. Considering the similar ionic radius and the same charge, the Bi^{3+} ions are most likely to occupy the Ca^{2+}, Lu^{3+} or Sc^{3+} sites. It is well known that there should be less than 30% ionic radius between the host ion and the dopant ion. As a result, it can be calculated using the equation below:

$$Dr = (Rm\,(CN) - Rd\,(CN))/(Rm\,(CN))$$

where Dr is the percentage of the radius difference, and Rm (CN) and Rd (CN) are the radii of the host ion and the doped ion, respectively. The calculated percentages of the Bi^{3+} ions occupying the sites of host cations Ca^{2+}, Lu^{3+} and Sc^{3+} are less than 30%. Considering the charge effects, Sc^{3+}, Lu^{3+} and Bi^{3+} have the same charge and Ca^{2+} does not match with the Bi^{3+} charge, and Bi^{3+} should prefer to occupy the Sc^{3+} and Lu^{3+} sites.

The scanning electron microscopy (SEM) and high-resolution transmission electron microscopy (HRTEM) images of the representative CLZSAG:0.14Bi^{3+} phosphor is shown in Fig. 1d. It can be seen from the SEM that the sample is composed of several micrometers, with irregular shapes but a smooth surface. The average particle size is estimated to be about 10 μm. By analyzing the element mapping image and energy dispersive X-ray spectroscopy (EDS) spectra, Ca, Lu, Sc, Zr, Al, Ge, O and Bi elements are uniformly distributed in the particles, which also further proves that the Bi^{3+} ions were successful incorporated into host materials. As shown in Fig. 1e, sharp diffraction spots can be found in the electron diffraction pattern of the selected region, and the corresponding interplanar distances of (211) and (321) are 0.614 and 0.318 nm, respectively.

Luminescence properties

Fig. 2 shows the diffuse reflection (DR) spectra of CLZSAG and CLZSAG:0.14Bi^{3+} samples. There is an obvious broadband
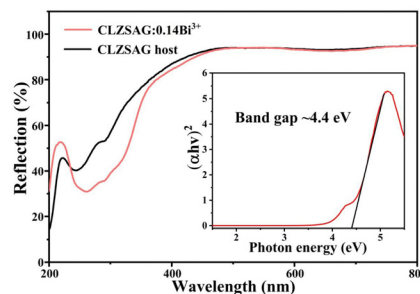
Fig. 2 DR spectra of the CLZSAG host and CLZSAG:0.14Bi^{3+} phosphors (the inset shows the calculated optical band gap values of the CLZSAG host based on the DR spectra).

absorption band in the range of 200–400 nm, which corresponds to the $^1S_0 \to {}^3P_1$ (300–400 nm) and $^1S_0 \to {}^1P_1$ (200–300 nm) transitions of the Bi^{3+} ions. The optical band gap can be calculated using the formula:[41]

$$F(R) = \frac{(1 - R^2)}{2R} \quad (1)$$

$$[F(R)h\nu]^n = D(h\nu - E_g) \quad (2)$$

where R is the reflectivity coefficient determined by the DR spectra, D is a constant, $h\nu$ is the photon energy, E_g is the optical band gap value, and the value of n corresponds to different transition types (direct transition n = 2 and indirect transition n = 1/2). The band gap of CLZSAG is calculated to be 4.4 eV. Therefore, CLZSAG is a suitable host that can accommodate the doped ion Bi^{3+} as luminescent materials.

It is widely known that Bi^{3+} has an electronic configuration of [Xe] 4f^{14}5d^{10}6s^2, and the free Bi^{3+} ions are very sensitive to the crystal field and are susceptible to the influence of the matrix material to emit different colors.[42–44] As shown in Fig. 3, different bands are composed in the spectrum by transitions from the ground state to the excited states as the $^3P_0$, $^3P_1$, $^3P_2$ and $^1P_1$ states (in order of increasing energy).[45] Among them, the transitions of $^1S_0 \to {}^3P_0$ and $^1S_0 \to {}^3P_2$ are spin forbidden and crystal field forbidden transition, so the absorption band in the 200–400 nm range can only be produced by the $^1S_0 \to {}^3P_1$ and
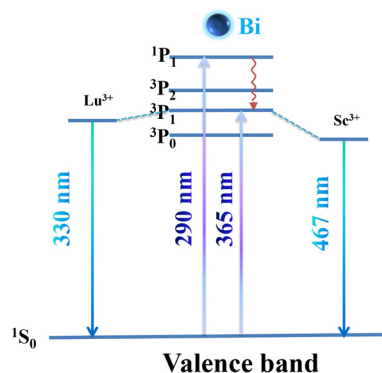
Fig. 3 The energy level diagram of Bi^{3+}.

$^1S_0 \to {}^1P_1$ transition.[46,47] The excited electrons in the $^1P_1$ energy level are transferred to the $^3P_1$ energy level by the nonradioactive transition. The matrix environment affects Bi^{3+} to induce crystal field splitting, and the stronger crystal field causes a lower $^3P_1$ energy level, resulting in a redshift in the emission band. Finally, the excited electrons return to the ground state *via* radiative transitions from the $^3P_1$ energy level, while releasing light.[48,49]

The photoluminescence emission (PL) and excitation (PLE) spectra of the prepared CLZSAG:$0.14Bi^{3+}$ at room temperature are shown in Fig. 4a. When monitored at 467 nm, the two excitation bands of CLZSAG:$0.14Bi^{3+}$ are observed at $\sim$290 and $\sim$365 nm, attributed to the $^1S_0 \to {}^1P_1$ and $^1S_0 \to {}^3P_1$ transition of Bi^{3+}. Under 290 nm excitation, two narrow emission band peaks at 330 (FWHM = 33 nm) and 467 nm (FWHM = 67 nm) were observed, which can be attributed to the $^3P_1 \to {}^1S_0$ transition of the Bi^{3+} ions. Under the excitation of 365 nm, a blue light emission band at 467 nm displays in the visible region of 400–700 nm. Furthermore, the excitation of the prepared blue-emitting luminescent material CLZSAG:$0.14Bi^{3+}$ matched well with the emission of the commercial near-UV 365 nm chips and can be used to develop high-performance WLEDs.

In order to investigate the local crystal environment of the Bi^{3+} emitting centers in the CLZSAG host, it is crucial to determine the crystal field strength of the Lu/Sc sites. The following equation can be used to calculate the crystal field strength (D_q):[50]

$$D_q = \frac{Ze^2 r^4}{6R^5} \tag{3}$$

The longer the bond length, the weaker the crystal field and lead to a shorter emission wavelength.[5] The average bond lengths of Sc–O and Lu–O are 2.09 Å and 2.52 Å, respectively.

Therefore, the crystal field strength of the Lu^{3+} site is lower than that of the Sc^{3+} site. On the basis of the preceding discussion, the 330 nm emission band comes from the Bi^{3+} ions occupying the Lu^{3+} sites and the 467 nm emission band results from the Bi^{3+} ions in the Sc^{3+} sites. The FWHM of emission spectra at 7 K became narrower (Fig. 4c), due to the decrease in electron–phonon interactions at lower temperatures.

The naked 6s and 6p electrons of Bi^{3+} are very sensitive to the local environment.[43,51] $[LuO_8]$ is surrounded by $[(Al/Ge)O_4]$ tetrahedra and $[(Sc/Zr)O_6]$ octahedra, making the Bi^{3+} activators in a very symmetric and compact microenvironment, which effectively limits the broadening of the emission band.[52] Thus, CLZSAG:Bi^{3+} shows a relatively narrow band (FWHM = 34 nm) at 330 nm, which is significantly narrower than most other Bi^{3+}-doped phosphors such as $K_2ZrSi_2O_7$ (125 nm) and $Ca_3Ga_4O_9$ (96 nm).[53,54] Intriguingly, the Stokes shift of CLZSAG:Bi^{3+} was calculated to be about 4179 cm^{-1} based on the excitation band at 290 nm and the emission band at 330 nm, which is smaller than those reported for most Bi^{3+}-activated phosphors.[42,55] Such a small Stokes shift indicates that it may have high efficiency and narrow emission bands.

We also investigated the relationship between the Bi^{3+} concentration and the PL intensity to determine the optimal doping amount. Normally, Bi^{3+}-activated phosphors exhibit a low quenching concentration. As shown in Fig. 1c, it can be seen that the distances between adjacent Lu^{3+} sites and Sc^{3+} sites are 3.81 and 6.22 Å, respectively. The small distance between the Bi^{3+} and Lu^{3+} sites facilitates the concentration quenching effect, corresponding to a lower critical quenching concentration of 6%. While the longer distance between the Bi^{3+} and Sc^{3+} sites can effectively suppress this effect and obtain a higher critical quenching concentration of 14%. As shown in Fig. 4b and d, the PL emission intensity reaches a maximum at
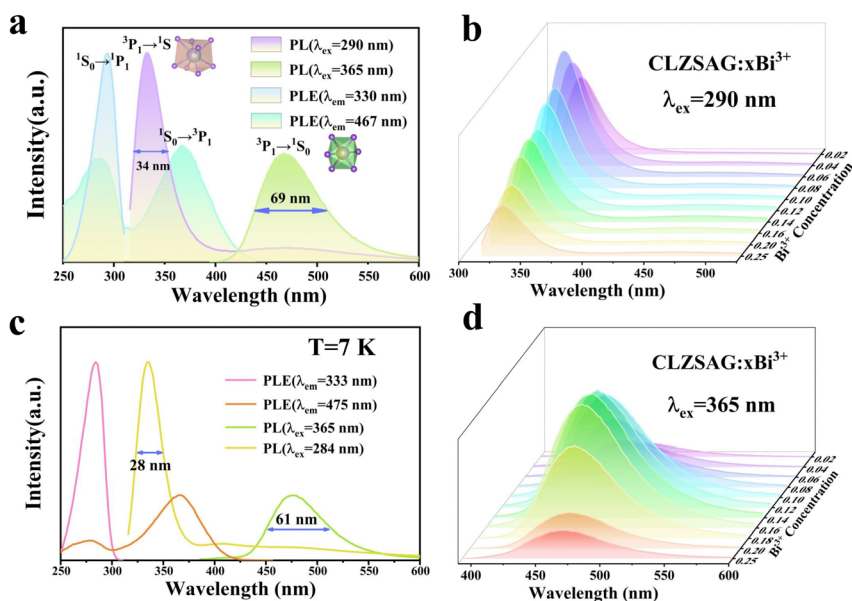

Fig. 4 (a) PLE and PL spectra of CLZSAG:$0.14Bi^{3+}$. (b) The PL spectra of CLZSAG:xBi^{3+} ($0.02 \leq x \leq 0.25$) under the excitation of 365 nm. (c) The emission spectrum of the CLZSAG:Bi^{3+} phosphor measured at 10 K. (d) The PL spectra of CLZSAG:xBi^{3+} ($0.02 \leq x \leq 0.25$) under the excitation of 290 nm.

This journal is © The Royal Society of Chemistry 2023

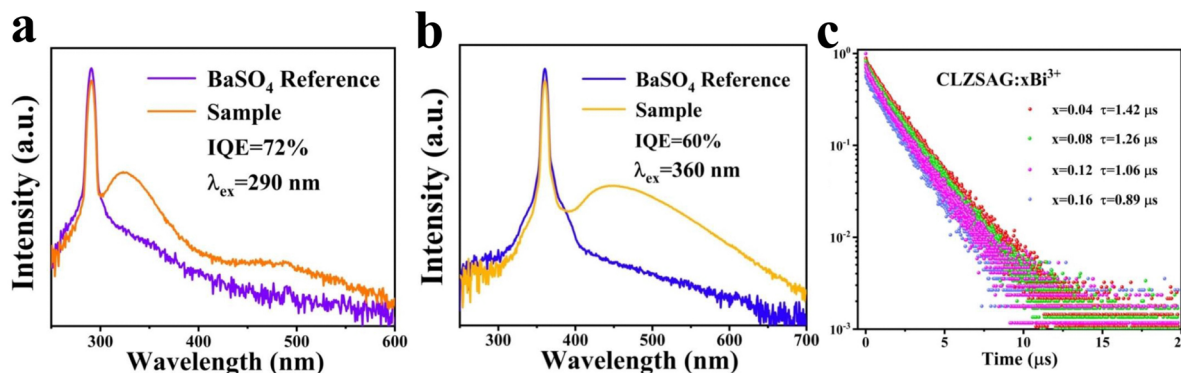*J. Mater. Chem. C*, 2023, **11**, 8818–8825 | **8821**

Fig. 5 (a) IQE of the CLZSAG:0.06Bi^{3+} phosphor under 290 nm excitation. (b) IQE of the CLZSAG:0.14Bi^{3+} phosphor under 360 nm excitation. (c) PL decay curves of CLZSAG:xBi^{3+} at room temperature (λ_{ex} = 375 nm, λ_{em} = 467 nm).

x = 0.06 with an increasing Bi^{3+} doping concentration under the excitation of 290 nm. And the optimal Bi^{3+} doping concentration is 14% under 365 nm light excitation. The emission intensity starts to decrease with the further increase of the Bi^{3+} doping concentration due to the concentration quenching effect. Moreover, the absorption of CLZSAG:0.14Bi^{3+} matches well with the 365 nm near-UV chips, indicating that it can be used to develop high-performance WLED devices.

Quantum efficiency is one of the important criteria to evaluate the performance of phosphors. The narrow emission band intensity of 330 nm is much stronger than that of 467 nm, and the Stokes shift is also relatively smaller, indicating a relatively higher quantum efficiency. As shown in Fig. 5, the CLZSAG:Bi^{3+} phosphor exhibited excellent quantum efficiencies, where the quantum efficiencies were 72% under 290 nm light excitation and 60% under 360 nm excitation. Compared with blue phosphors RbNa$_3$(Li$_3$SiO$_4$)$_4$:Eu^{2+} (IQE = 53%, EQE = 13%),[56] the CLZSAG:Bi^{3+} phosphors exhibit a higher quantum efficiency, revealing its great potential application for WLEDs.

For practical applications, the decay behavior in the host material is a critical component. The decay curves of CLZSAG:xBi^{3+} were measured at room temperature (Fig. 5c). The average decay time τ are calculated according to the following equation:

$$\tau = \frac{\int_{\infty}^{0} tI(t)dt}{\int_{\infty}^{0} I(t)dt} \tag{4}$$

Therefore, the τ values of Bi^{3+} are estimated to be 1.75, 1.73, 1.67, 1.66, and 1.57 μs respectively, corresponding to concentrations x of 0.02, 0.06, 0.08, 0.10, and 0.14. The decay time decreases with the increase of the CLZSAG:xBi^{3+} concentration due to the energy transfer between Bi^{3+} ions.

Temperature dependence of Bi^{3+} luminescence

Thermal stability is an essential feature for phosphors used in high-power LEDs, because the operating temperature can reach up to 423 K due to the long-term operation. Fig. 6a and b depict the temperature dependent spectra of the CLZSAG:0.14Bi^{3+} phosphor, and the PL emission intensity (λ_{ex} = 365 nm) gradually decreases with the increment of temperature due to the

quenching effect, but the intensity still maintains 80% at 423 K, compared with the emission intensity at room temperature. CLZSAG:0.14Bi^{3+} exhibits excellent thermal stability which is better than many other reported blue-emitting phosphors, such as MgAl$_2$Si$_4$O$_6$N$_4$:Eu^{2+} (I_{423K}/I_{298K} = 65%),[57] ScCaOBO$_3$:Ce^{3+} (I_{423K}/I_{298K} = 21%),[58] BaLa$_2$Si$_2$S$_8$:Ce^{3+} (I_{423K}/I_{298K} = 20%)[34] and Ca$_4$HfGe$_3$O$_{12}$:Bi^{3+} (I_{423K}/I_{298K} = 51%).[59] As the temperature increases, the interaction between electrons and phonons is enhanced. The excited electrons gain phonon energy through nonradiative relaxation to overcome the energy barrier, leading to thermal quenching. The activation energy (ΔE) is what is meant by the term "energy barrier", and the higher the activation energy, the weaker the thermal quenching is. We calculate the activation energy (ΔE) using the Arrhenius formula:[49,60]

$$I = \frac{I_0}{1 + Ae^{-\frac{\Delta E}{kT}}} \tag{5}$$

where I_0 and I denote the initial and integral PL intensities at temperature T, A is a constant, and k represents the Boltzmann constant ($k = 8.617 \times 10^{-5}$ eV K^{-1}). Through the connection of linear fitting $\ln[(I_0/I) - 1]$ *vs.* $1/kT$, the value of ΔE was determined to be 0.21 eV (Fig. 6c).

Moreover, the temperature-dependent spectra of CLZSAG:Bi^{3+} have been measured and investigated. As shown in Fig. 6a and d, it can be seen that there is no obvious change of the emission peak with the increase of temperature, while the FWHM of the emission spectrum is slightly broadened which can be due to the electron–phonon interaction. These results demonstrate that the obtained sample has great thermal stability, which can meet the requirement of high-power WLEDs.

Application in pc-WLEDs

To explore the application potential of the as-prepared CLZSAG:Bi^{3+} phosphors, we prepared WLED devices using 365 nm near-UV chips in combination with commercial yellow-green powder LuYAG:Ce^{3+}, red powder CaAlSiN$_3$:Eu^{2+} and as-prepared CLZSAG:Bi^{3+} samples. Fig. 7 shows the electroluminescence spectrum and the Commission International deI' Eclairage (CIE) coordinate is (0.3531, 0.3694). The inset
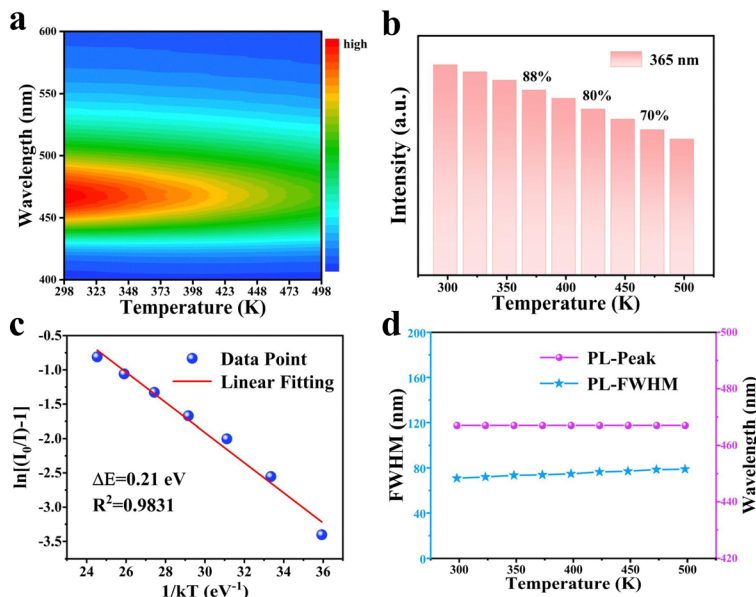
8822 | *J. Mater. Chem. C*, 2023, **11**, 8818–8825

This journal is © The Royal Society of Chemistry 2023

Fig. 6 (a) Contour maps of the emission spectra of the temperature variation of CLZSAG:0.14Bi^{3+} (λ_{ex} = 365 nm). (b) Normalized integrated intensity with temperature for CLZSAG:0.14Bi^{3+}. (c) Linear fittings of the relationship between ln $[(I_0/I) - 1]$ with a $1/kT$ of CLZSAG:0.14Bi^{3+}. (d) The temperature-dependent of the PL peak position and FWHM.
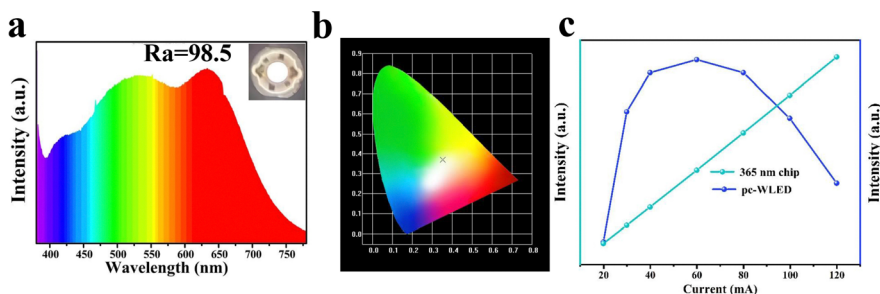

Fig. 7 (a) Electroluminescence spectrum of WLEDs fabricated with blue phosphor CLZSAG:0.14Bi^{3+}, yellow phosphor LuYAG:Ce^{3+}, and red phosphor CaAlSiN$_3$:Eu^{2+} at 10 mA driving current. (b) CIE chromaticity coordinate of the as-prepared WLED device. (c) Dependence of the relative emission intensity of the CLZSAG:Bi^{3+}, LuYAG:Ce^{3+} and CaAlSiN$_3$:Eu^{2+} coated LED devices and the 365 nm chip at a direct current in the range of 20–120 mA.

shows an image of the working WLED device taken in the dark. As can be observed in Fig. 7c, the emission intensity begins to increase as the current increases, peaking at 60 mA, due to the increases in the intensity of the stimulated light. As the current increases further ($>$ 60 mA), the emission intensity decreases, which may come from the thermal quenching of the phosphor. Table 2 lists the CIE color coordinates, CCT, and CRI

dependence curves for WLED devices with respect to operating currents. It is remarkable that the WLED has an ultra-high color rendering index (R_a = 98.5) and a low correlation color temperature (CCT = 4455 K) and the luminous efficiency is 24.5 lm W^{-1} at 10 mA driving current. The CRI index increases from 82 to 98.5 compared with the WLED device fabricated by LuYAG:Ce^{3+}, CaAlSiN$_3$:Eu^{2+} and a blue chip mentioned in the reference (R_a > 80, CCT > 4500 K).[22] This result indicates that the prepared CLZSAG:Bi^{3+} phosphors have great potential applications in high-performance warm WLEDs.

Conclusions

In this study, a novel series of CLZSAG:Bi^{3+} phosphors with a garnet structure were synthesized by using a high-temperature solid-state reaction. CLZSAG:Bi^{3+} phosphors exhibit blue light emission under 365 nm excitation and a rare ultra-narrow UV-emission band (FWHM = 34 nm) under 290 nm excitation. The

Table 2 Chromaticity parameters of the as-manufactured WLED devices at 10–120 mA drive current

Type	Current (mA)	CIE coordinates	CCT (K)	CRI
pc-WLED	10	0.3531, 0.3694	4455 K	98.5
	20	0.3505, 0.3680	4872 K	96.0
	40	0.3452, 0.3614	5030 K	93.8
	60	0.3436, 0.3576	5077 K	92.1
	80	0.3422, 0.3547	5119 K	90.9
	100	0.3420, 0.3531	5122 K	90.0
	120	0.3412, 0.3511	5152 K	89.4

CLZSAG:Bi^{3+} phosphors also have excellent thermostability ($I_{423K/298K}$ = 80%) and a high quantum efficiency of 60% under 365 nm excitation. The CLZSAG:Bi^{3+} phosphors emit bright light and can be used as a component of blue emission phosphors. The pc-WLED device was created by fusing blue CLZSAG:Bi^{3+}, LuYAG:Ce^{3+}, and CaAlSiN$_3$:Eu^{2+} with a 365 nm near-UV chip with a high color rendering index (R_a = 98.5) and a low correlated color temperature (CCT = 4455 K). These characterics demonstrate that the CLZSAG:Bi^{3+} phosphors have potential applications for WLED technology stimulated by near-UV light.

Conflicts of interest

The authors declare no conflicts of interest.

Acknowledgements

References

1 X. Pan, L. Mei, Y. Zhuang, T. Seto, Y. Wang, M. Plyaskin, W. Xi, C. Li, Q. Guo and L. Liao, *Chem. Eng. J.*, 2022, **434**, 134652.

2 B. Shao, J. Huo and H. You, *Adv. Opt. Mater.*, 2019, **7**, 1900319.

3 H. Yuan, F. Massuyeau, N. Gautier, A. B. Kama, E. Faulques, F. Chen, Q. Shen, L. Zhang, M. Paris and R. Gautier, *Angew. Chem., Int. Ed.*, 2020, **59**, 2802–2807.

4 C. C. Lin, Y.-T. Tsai, H. E. Johnston, M.-H. Fang, F. Yu, W. Zhou, P. Whitfield, Y. Li, J. Wang, R.-S. Liu and J. P. Attfield, *J. Am. Chem. Soc.*, 2017, **139**, 11766–11770.

5 L. Dong, L. Zhang, Y. Jia, B. Shao, W. Lü, S. Zhao and H. You, *ACS Sustainable Chem. Eng.*, 2020, **8**, 3357–3366.

6 P. Pust, P. J. Schmidt and W. Schnick, *Nat. Mater.*, 2015, **14**, 454–458.

7 J. Qiao, L. Ning, M. S. Molokeev, Y. C. Chuang, Q. Zhang, K. R. Poeppelmeier and Z. Xia, *Angew. Chem., Int. Ed.*, 2019, **58**, 11521–11526.

8 M. Peng, X. Yin, P. A. Tanner, M. G. Brik and P. Li, *Chem. Mater.*, 2015, **27**, 2938–2945.

9 S. Liang, M. Shang, H. Lian, K. Li, Y. Zhang and J. Lin, *J. Mater. Chem. C*, 2016, **4**, 6409–6416.

10 J. Wang, L. Dong, Z. Lyu, D. Sun, T. Tan and H. You, *Adv. Funct. Mater.*, 2023, 2214611, DOI: **10.1002/adfm.202214611.**

11 L. Dong, L. Zhang, Y. Jia, B. Shao, W. Lu, S. Zhao and H. You, *ACS Appl. Mater. Interfaces*, 2020, **12**, 7334–7344.

12 S. Li, L. Wang, N. Hirosaki and R. J. Xie, *Laser Photonics Rev.*, 2018, **12**, 1800173.

13 Y. Wang, J. Ding, Y. Wang, X. Zhou, Y. Cao, B. Ma, J. Li, X. Wang, T. Seto and Z. Zhao, *J. Mater. Chem. C*, 2019, **7**, 1792–1820.

14 X. Ma and Y. Wang, *Adv. Opt. Mater.*, 2023, 2202765, DOI: **10.1002/adom.202202765.**

15 R. Shi, X. Zhang, Z. Qiu, J. Zhang, S. Liao, W. Zhou, X. Xu, L. Yu and S. Lian, *Inorg. Chem.*, 2021, **60**, 19393–19401.

16 J. Han, L. Li, M. Peng, B. Huang, F. Pan, F. Kang, L. Li, J. Wang and B. Lei, *Chem. Mater.*, 2017, **29**, 8412–8424.

17 Z. Xia and Q. Liu, *Prog. Mater. Sci.*, 2016, **84**, 59–117.

18 L. Sun, B. Devakumar, J. Liang, S. Wang, Q. Sun and X. Huang, *J. Mater. Chem. C*, 2020, **8**, 1095–1103.

19 J. Hye Oh, S. Ji Yang and Y. Rag Do, *Light: Sci. Appl.*, 2014, **3**, e141–e141.

20 P. Dang, Q. Zhang, D. Liu, G. Li, H. Lian, M. Shang and J. Lin, *Chem. Eng. J.*, 2021, **420**, 127640.

21 J. Liang, B. Devakumar, L. Sun, S. Wang, Q. Sun and X. Huang, *J. Mater. Chem. C*, 2020, **8**, 4934–4943.

22 C. Zhong, L. Zhang, Y. Xu, X. Wu, S. Yin, X. Zhang and H. You, *Mater. Today Chem.*, 2022, **26**, 101233.

23 Q. Wei, J. Ding, H. Chen, Q. Zhang and Y. Wang, *Chem. Eng. J.*, 2020, **385**, 123392.

24 Q. Zhang, X. Wang and Y. Wang, *Inorg. Chem. Front.*, 2020, **7**, 1034–1045.

25 J. Han, F. Pan, M. S. Molokeev, J. Dai, M. Peng, W. Zhou and J. Wang, *ACS Appl. Mater. Interfaces*, 2018, **10**, 13660–13668.

26 Y. Li, S. Qi, P. Li and Z. Wang, *RSC Adv.*, 2017, **7**, 38318–38334.

27 X. Huang, J. Liang, S. Rtimi, B. Devakumar and Z. Zhang, *Chem. Eng. J.*, 2021, **405**, 126950.

28 G. E. Wang, G. Xu, M. S. Wang, L. Z. Cai, W. H. Li and G. C. Guo, *Chem. Sci.*, 2015, **6**, 7222–7226.

29 G. Li, Y. Tian, Y. Zhao and J. Lin, *Chem. Soc. Rev.*, 2015, **44**, 8688–8713.

30 Y. Xu, L. Zhang, S. Yin, X. Wu and H. You, *J. Alloys Compd.*, 2022, **911**, 165149.

31 Z. Leng, H. Bai, Q. Qing, H. He, J. Hou, B. Li, Z. Tang, F. Song and H. Wu, *ACS Sustainable Chem. Eng.*, 2022, **10**, 10966–10977.

32 T. Hasegawa, M. Iwaki, S. W. Kim, T. Ueda, K. Uematsu, K. Toda and M. Sato, *J. Alloys Compd.*, 2019, **797**, 1181–1189.

33 T. Hasegawa, S. W. Kim, T. Ueda, T. Ishigaki, K. Uematsu, H. Takaba, K. Toda and M. Sato, *J. Mater. Chem. C*, 2017, **5**, 9472–9478.

34 S. P. Lee, C. H. Huang, T. S. Chan and T. M. Chen, *ACS Appl. Mater. Interfaces*, 2014, **6**, 7260–7267.

35 C. Yan, Z. Liu, W. Zhuang, R. Liu, X. Xing, Y. Liu, G. Chen, Y. Li and X. Ma, *Inorg. Chem.*, 2017, **56**, 11087–11095.

36 Y.-C. Lin, M. Bettinelli and M. Karlsson, *Chem. Mater.*, 2019, **31**, 3851–3862.

37 P. Dang, W. Wang, H. Lian, G. Li and J. Lin, *Adv. Opt. Mater.*, 2022, **10**, 2102287.

38 J. Xue, Z. Yu, H. M. Noh, B. R. Lee, B. C. Choi, S. H. Park, J. H. Jeong, P. Du and M. Song, *Chem. Eng. J.*, 2021, **415**, 128977.

39 X. Zhang, L. Dong, L. Zhang, Y. Xu, X. Wu, S. Yin, C. Zhong and H. You, *J. Mater. Chem. C*, 2022, **10**, 16857–16864.

8824 | *J. Mater. Chem. C*, 2023, **11**, 8818–8825

This journal is © The Royal Society of Chemistry 2023

40 X. Zhang, L. Zhang, Y. Xu, X. Wu, S. Yin, C. Zhong and H. You, *Inorg. Chem.*, 2022, **61**, 7597–7607.

41 Y. Zheng, W. Zhuang, X. Xing, J. Zhong, R. Liu, Y. Li, Y. Liu and Y. Hu, *RSC Adv.*, 2016, **6**, 68852–68859.

42 Y. Tang, M. Deng, M. Wang, X. Liu, Z. Zhou, J. Wang and Q. Liu, *Adv. Opt. Mater.*, 2022, **11**, 2201827.

43 D. Liu, X. Yun, P. Dang, H. Lian, M. Shang, G. Li and J. Lin, *Chem. Mater.*, 2020, **32**, 3065–3077.

44 Y. Wei, Z. Gao, X. Yun, H. Yang, Y. Liu and G. Li, *Chem. Mater.*, 2020, **32**, 8747–8753.

45 Q. Wu, Y. Li, Y. Wang, H. Liu, S. Ye, L. Zhao, J. Ding and J. Zhou, *Chem. Eng. J.*, 2020, **401**, 126130.

46 P. Dang, D. Liu, G. Li, A. A. Al Kheraif and J. Lin, *Adv. Opt. Mater.*, 2020, **8**, 1901993.

47 Z. Zhou, X. Wang, X. Yi, H. Ming, Z. Ma and M. Peng, *Chem. Eng. J.*, 2021, **421**, 127820.

48 Y. Wei, W. Wang, Z. Wang, H. Yang, X. You, Y. Zhao, P. Dang, H. Lian, J. Hao, G. Li and J. Lin, *Adv. Funct. Mater.*, 2022, **33**, 2205829.

49 S. Wu, P. Xiong, X. Liu, Y. Fu, Q. Liu, M. Peng, Y. Chen and Z. Ma, *J. Mater. Chem. C*, 2020, **8**, 16584–16592.

50 P. Dang, S. Liang, G. Li, Y. Wei, Z. Cheng, H. Lian, M. Shang, S. J. Ho and J. Lin, *J. Mater. Chem. C*, 2018, **6**, 6449–6459.

51 H. Li, R. Pang, Y. Luo, H. Wu, S. Zhang, L. Jiang, D. Li, C. Li and H. Zhang, *ACS Appl. Electron. Mater.*, 2019, **1**, 229–237.

52 S. Wang, H. Wu, Y. Fan, Q. Wang, T. Tan, R. Pang, S. Zhang, D. Li, L. Jiang, C. Li and H. Zhang, *Chem. Eng. J.*, 2022, **432**, 134265.

53 D.-Y. Wang, Z.-B. Tang, W. U. Khan and Y. Wang, *Chem. Eng. J.*, 2017, **313**, 1082–1087.

54 D. Liu, X. Yun, G. Li, P. Dang, M. S. Molokeev, H. Lian, M. Shang and J. Lin, *Adv. Opt. Mater.*, 2020, **8**, 2001037.

55 P. Boutinaud, *Inorg. Chem.*, 2013, **52**, 6028–6038.

56 H. Liao, M. Zhao, M. S. Molokeev, Q. Liu and Z. Xia, *Angew. Chem., Int. Ed.*, 2018, **57**, 11728–11731.

57 Y. Liu, Y. Liu, M. Wu, C. He, Q. Liu, X. Huang, X. Min, Z. Huang, H. Wang and R. Mi, *Dalton Trans.*, 2022, **51**, 16639–16647.

58 W. Wang, T. Tan, S. Wang, S. Zhang, R. Pang, D. Li, L. Jiang, H. Li, C. Li and H. Zhang, *Mater. Today Chem.*, 2022, **26**, 101030.

59 S. Piao, Y. Wang, G. Zhu, J. Zhang, X. Zhang, D. Wu, Y. Cao, X. Li and B. Chen, *J. Mater. Chem. C*, 2021, **9**, 14777–14787.

60 P. Xiong, M. Peng, K. Qin, F. Xu and X. Xu, *Adv. Opt. Mater.*, 2019, **7**, 1901107.